Communication

MR measurement of critical phase transition dynamics and supercritical fluid dynamics in capillary and porous media flow

Erik M. Rassi [a], Sarah L. Codd [a,*], Joseph D. Seymour [b]

[a] Mechanical and Industrial Engineering Dept., Montana State University, Bozeman, MT, USA
[b] Dept. of Chemical and Biological Engineering, Montana State University, Bozeman, MT, USA

ABSTRACT

Supercritical fluids (SCF) are useful solvents in green chemistry and oil recovery and are of great current interest in the context of carbon sequestration. Magnetic resonance techniques were applied to study near critical and supercritical dynamics for pump driven flow through a capillary and a packed bed porous media. Velocity maps and displacement propagators measure the dynamics of C_2F_6 at pressures below, at, and above the critical pressure and at temperatures below and above the critical temperature. Displacement propagators were measured at various displacement observation times to quantify the time evolution of dynamics. In capillary flow, the critical phase transition fluid C_2F_6 showed increased compressibility compared to the near critical gas and supercritical fluid. These flows exhibit large variations in buoyancy arising from large changes in density due to very small changes in temperature.

© 2011 Elsevier Inc. All rights reserved.

1. Introduction

Supercritical fluids (SCF) are widely used for chromatography applications, green chemistry and solvents [1]. Supercritical extraction processes are increasingly used in oil recovery and in carbon sequestration applications [2–5]. The flow dynamics of supercritical fluids has motivated work on the theoretical aspects [6–14], but the field remains experimentally limited with a few exceptions [15–17]. Hexafluoroethane (C_2F_6) was pumped at 0.5 mL/min in a cylindrical tube through a magnetic resonance (MR) spectrometer where propagators and velocity maps were measured at temperatures above the critical temperature and at pressures below, at, and above the critical pressure. In capillaries, it was observed that flow of C_2F_6 with properties far above or below the critical point had a Poiseuille flow distribution consistent with ordinary Newtonian fluid behavior of liquid and gas flows. Flows with properties near the critical point had flow distributions strongly impacted by buoyancy and viscous forces. Additionally, C_2F_6 was pumped at 0.5 mL/min in a cylindrical packed bed of 55 µm beads. The MR measured propagators and velocity maps provide the first non-invasive characterization of transport dynamics for a flowing supercritical fluid in a porous media. The flow loop designed specifically for integration with the MR magnet and high pressure controlled flow function is presented.

A supercritical fluid is a fluid that is above its critical temperature, pressure, and density [18]. A fluid in this state has properties similar to gases and liquids. For instance, a SCF has transport properties such as diffusivities and viscosities similar to the gas phase while densities resemble the liquid phase. The fact that the material properties of a SCF are sensitive to temperature and pressure can be exploited for chemical processing. The specific heat, density, viscosity, and heat transfer coefficients can be controlled over wide ranges [19]. Experimentally, the effects of the thermophysical properties of a supercritical fluid under pressure driven flow against and with gravity have been well studied [20]. At a threshold determined by the ratio of buoyant to viscous forces, *i.e.* the Rayleigh number, buoyancy in the fluid begins to impact the heat transfer and mass transport. Much work has been performed to numerically or theoretically [21] predict and validate the thermophysical behavior of near critical fluids including buoyancy effects [8–11]. Recently focus has shifted from larger scale experiments to small capillaries [22] and porous tubes [19,23]. Work thus far has validated numerical and theoretical models with thermophysical experimental data, but hydrodynamic data is very limited. In regards to velocity distributions of a flowing fluid near the critical point, several groups developed theoretical or numerical models for turbulent or laminar entrance flows [19,21], but again limited experimental data is available [15,17]. Currently available velocity data was acquired using invasive methods, such as Pitot tubes. The experimental MR velocity maps presented in this paper provide non-invasive spatially encoded velocity in a SCF.

* Corresponding author. Fax: +1 406 994 5308.
E-mail address: scodd@coe.montana.edu (S.L. Codd).

Prior MR research has included non-flowing SCF's (n-Pentane) in porous media composed of Vycor glass with pore diameters of $\sim$6 nm and crushed into particle sizes of $\sim$500 μm where it was shown that the critical temperature inside the Vycor pores was lowered relative to the bulk fluid and was impacted by the void size between the particles [24,25]. MR imaging has been used to obtain signal intensity and relaxation components of supercritical CO_2 dissolved in water in a porous Berea sandstone [26]. The signal from the supercritical CO_2 was not directly measured. Instead, the signal from water and deuterium oxide was measured as the CO_2 replaced the water in the sandstone pores. MR has also been used in supercritical fluid chromatography (SFC) using CO_2 as a solvent that did not interfere with NMR signal from the solute [2,3,27,28]. Another aspect of SCF's that has been studied is the magnetic relaxation as a function of the thermodynamic state [29] and molecular interactions [30]. T_1 relaxation of supercritical fluids increases with increasing pressure and decreases with increasing temperature but, the trend does not hold for near critical fluids. The T_1 relaxation of CO_2 dips near the critical point [31]. This behavior of the T_1 relaxation near the critical point is most likely caused by the fluctuation of density near the critical point [31].

Minimal quantitative data exists for flowing supercritical fluids. A significant need exists to study flowing SCF's due to the wide and expanding use for applications other than heat transfer. The first application of MR to flowing supercritical fluids with the purpose of obtaining flow dynamics is presented here.

2. Experimental

Magnetic resonance techniques [32–35] were used to obtain velocity maps, propagators, and diffusion coefficients over a range of pressures and MR displacement observation times for flow in either a capillary or a porous media bead pack. Hexafluoroethane, C_2F_6, was chosen for these studies due to its favorable combination of critical temperature T_c = 19.88 °C, critical pressure P_c = 30.48 bar (1 bar = 100 kPa) and MR relaxation times in the pressure range of 10–75 bar ($T_1 \sim$ 80–1240 ms, $T_2 \sim$ 80–1020 ms) as well as the high natural abundance and strong MR signal for ^{19}F [36–39]. Observations were made on stationary fluid and flowing fluid.

C_2F_6 was pumped through a system specifically designed for pressure driven flow control within a MR magnet (Fig. 1). From the supply tank, the gas was pumped at a range of pressures from the gas phase at 10 bar to SCF at 45 bar using an Isco 500D syringe pump. The Isco 500D provides a constant volumetric flow rate between .001 and 204 mL/min. C_2F_6 flowed through the MR system at a flow rate of 0.5 mL/min through 1.524 mm ID PEEK tubing and stainless steel tubing outside of the MR magnet. The flow rates for all data presented correspond to Reynolds numbers $Re = \frac{\rho \langle v \rangle D_{tube}}{\mu}$ of 50–200 indicating the flow is laminar (non turbulent).

Back pressure for the flow system was maintained by a Thar back pressure regulator APBR-20-1. The back pressure regulator maintains the absolute pressure of the system's exit, independent of flow rate. The back pressure regulator is equipped with a heated valve to eliminate freezing from the rapidly expanding gas. The gas was collected for reuse. Pressure transducers monitored the pressure of the fluid upstream and downstream of the MR magnet. The room temperature was also monitored and controlled with a precision of ±0.5 °C. The fluid temperature was equilibrated with room temperature for 1 h before experiments were run. MR data was collected using a 5 mm RF birdcage coil, an AVANCE III 300 MHz Spectrometer, and a Bruker Micro 2.5 three dimensional gradient probe capable of 1.48 T/m. The pulse sequence used for the velocity maps is shown in Fig. 2a and the sequence for the propagators is shown in Fig. 2b. The temperature of the air surrounding the capillary tube T_{surr} was controlled by the gradient cooling water and the fluid temperature T_{fluid} was controlled at the gas storage cylinder and temperatures were monitored by thermocouples.

The porous media bead pack was constructed from d_p = 55 ± 8.8 μm diameter copolymer microspheres (Thermo Scientific, 7550A) at porosity $\Phi \sim 0.44$ corresponding to a pore length scale $l_p = \frac{\Phi d_p}{(1-\Phi)} = 43.2$ μm. The packed bed length was 200 mm in PEEK 1.524 mm ID tubing. A velocity map of C_2F_6 flowing at 0.5 mL/min through the 55 μm bead pack contained in a 1.524 mm ID PEEK capillary at supercritical pressure P = 45 bar was measured. The velocity map pulse sequence had a displacement observation time Δ = 2.239 ms and gradient pulse duration δ = 0.25 ms. The stimulated echo was used due to the shorter T_2^* of the fluid in the porous media. No slice selection was used so the image is of the entire excitation region of the rf coil (length = 20 mm). The repetition time was T_R = 2 s and 32 signal averages were used for a total experiment time of 68 min. The spatial resolution with a field of view of 4 mm × 2 mm [64 × 32] was 62.5 μm × 62.5 μm.

Propagators characterize the hydrodynamic dispersion in porous media [40,41] and were measured for flowing C_2F_6 at 0.5 mL/min in the 55 μm beads at three pressures P = 25 bar, 29 bar, and 45 bar (Fig. 7). The propagator sequence Fig. 2b used a stimulated echo PGSE with displacement observation times in the range Δ = 50–500 ms and gradient pulse duration δ = 0.25 or 0.5 ms,
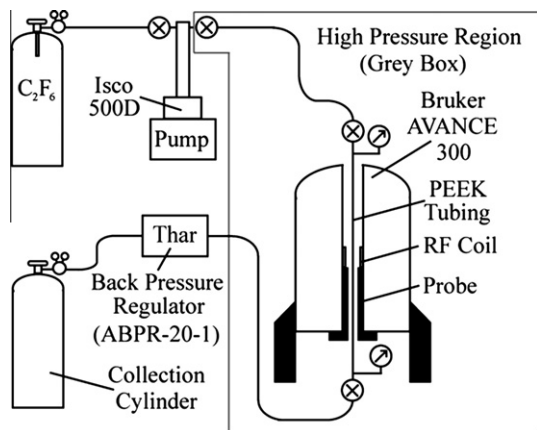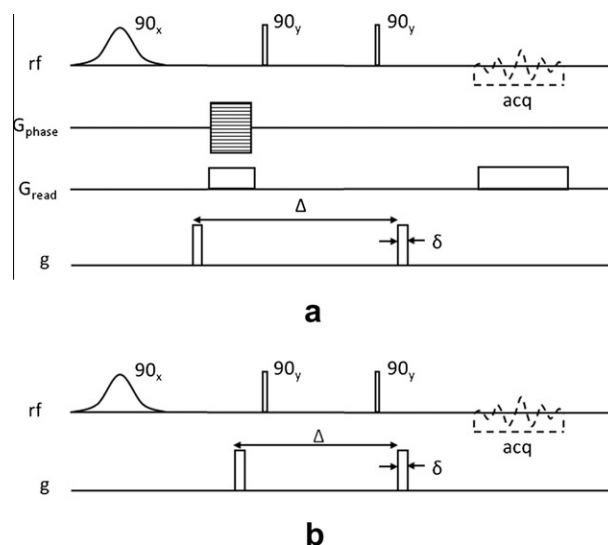

Fig. 1. Supercritical flow loop schematic.

Fig. 2. (a) Velocity map pulse sequence using a stimulated echo and (b) single pulsed gradient stimulated echo sequence for propagators.
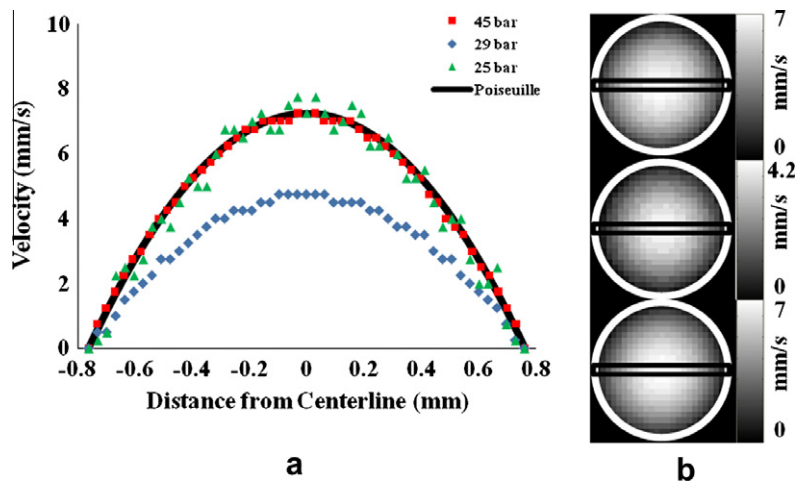
Fig. 3. (a) Velocity profiles of C_2F_6 at T_{fluid} = 21 °C and pressures P = 25, 29, and 45 bar for flow against gravity (upward) with T_{surr} = 21 °C. Image (b) contains the velocity maps corresponding to (a). The black rectangle is the cross section from which the profiles were taken.

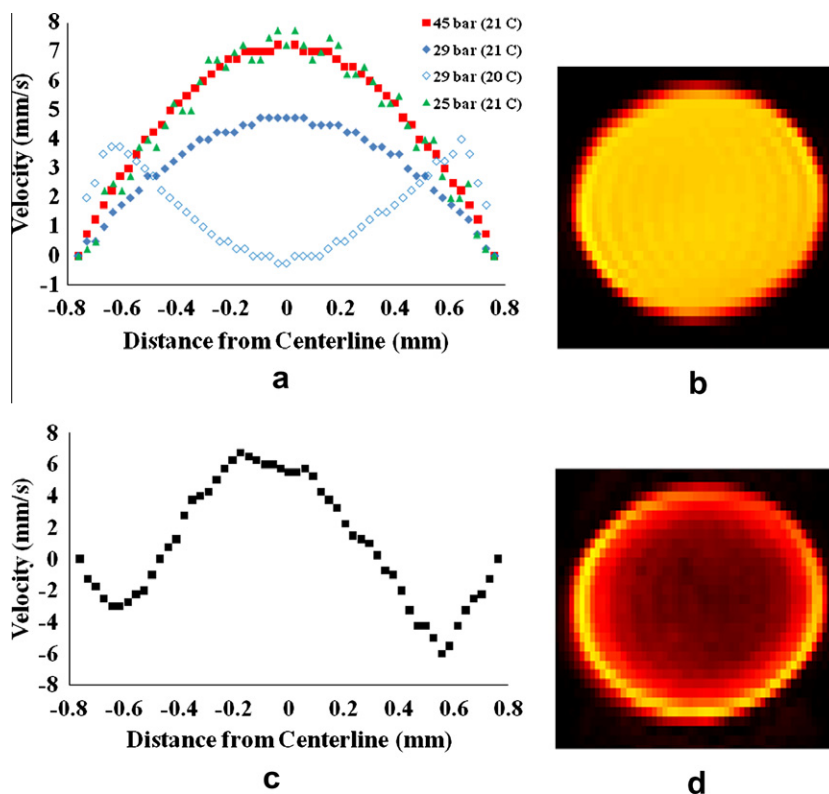**Fig. 4.** Shown in (a) are upward velocity profiles of C_2F_6 at pressures of 25, 29, 45 bar at T_{fluid} = 21 °C with T_{surr} = 21 °C. Test 29 bar (20 °C) had T_{fluid} = 20 °C with T_{surr} = 21 °C. This test was closer to the critical point temperature than the other 29 bar test. In (b) a density map for 45 bar at T_{fluid} = 21 °C with T_{surr} = 21 °C which was representative for all of the tests in (a). (c) Shows the velocity profile of two-phase flow at 29 bar with T_{fluid} = 19 °C, T_{surr} = 15 °C and (d) is the corresponding density map.

depending on the maximum gradient requirements for shorter displacement observation times. No slice selection was used, exciting the entire sample (approx. 20 mm length). The repetition time T_R = 2 s and 16 signal averages were taken for each pressure resulting in a data acquisition time of 67 min.

3. Results and discussion

3.1. Capillary flow

Velocity maps were taken at three pressures P = 25 bar a near critical gas, P = 29 bar a critical phase transition fluid, and

P = 45 bar a supercritical fluid and at fluid temperatures of T_{fluid} = 20 or 21 °C and at T_{surr} = 21 °C for upward flow against gravity (Figs. 3 and 4). The velocity measurements used an observation time Δ = 7.41 ms and a pulse duration δ = 0.5 ms. A 20 mm slice was excited. The in plane resolution was 62.5 μm × 62.5 μm. The number of averages was 128, 32, and 32 for P = 25, 29, and 45 bar, respectively due to signal increase with increasing fluid density. The repetition time T_R of 2 s resulted in a total experiment time of 272, 68, and 68 min for P = 25, 29, and 45 bar, respectively. The field of view (FOV) was 4 mm × 2 mm, corresponding to 64 × 32 points in the read and phase encoded directions. Data was analyzed in Prospa (Magritek, NZ) and a profile of the spatial
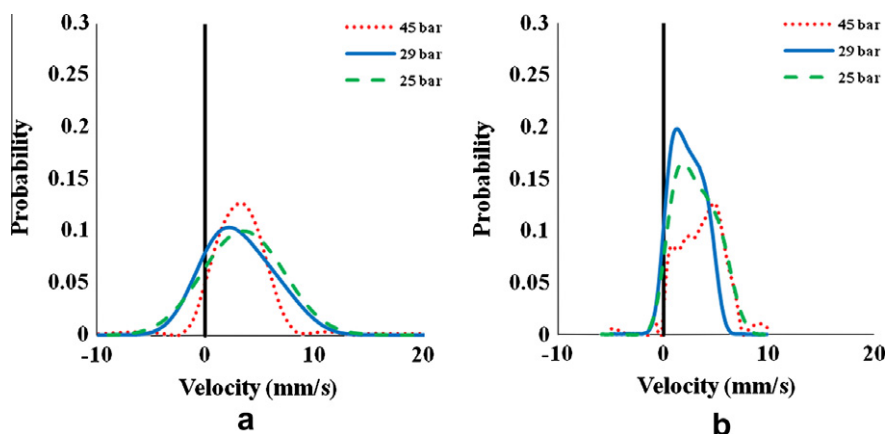
Fig. 5. Upward flow propagators of C_2F_6 at 25, 29, and 45 bar with T_{fluid} = 21 °C, T_{surr} = 21 °C, and at an observation time of (a) 10 ms and (b) 100 ms.

velocity distribution across the diameter of the tube was extracted for each pressure (Fig. 3).

From the velocity profiles the average velocity $\langle v \rangle$, which is half of the maximum velocity for the parabolic Poiseuille profile of a Newtonian fluid in laminar flow, for each pressure was determined: $\langle v \rangle$ = 3.63, 2.38, and 3.63 mm/s, for P = 25, 29, and 45 bar, respectively. The compressibility of the fluid flow at the critical point is clearly visible by the reduced maximum and average velocity of the P = 29 bar profile compared to 25 or 45 bar under constant volumetric flow. Flow of C_2F_6 near the critical point is highly compressible due to large density fluctuations, also responsible for the phenomena of critical opalescence in which mesoscale density variations on scales of ~500 nm scatter light at the critical point [13]. The critical phase transition is associated with a divergent correlation length for density fluctuations [1,7]. Flow nearest the critical point is very sensitive to thermal conditions and small temperature gradients can cause a large density gradient due to divergence of the thermal compressibility at the critical point [38]. As shown in Fig. 4a, for less than 1 °C difference between T_{surr} and T_{fluid} in the upward flow case near the critical point, the reduction of viscosity and density has caused the fluid near the walls to flow faster than that in the center of the tube causing an "M" shape velocity profile (Fig. 4a) [21].

A magnitude image (Fig. 4b) shows the spin density for 45 bar at T_{fluid} = 21 °C with T_{surr} = 21 °C and is homogeneous as are those for the other temperatures and pressures for which one expects a single phase. Spatial density fluctuations are smaller than the image resolution. Fig. 4c and d are the velocity profile and density map of the fluid below the supercritical temperature at T_{fluid} = 19 °C and T_{surr} = 15 °C in the two phase (gas–liquid) region of the phase diagram. Due to the colder wall temperature, the fluid condensed near the walls flowing downward in the liquid state, while the warmer fluid in the center of the tube flowed upward in the gaseous state. The density maps provide a convenient check of macroscopic fluid density homogeneity and clearly show the flow is two phase in the case of P = 29 bar with T_{fluid} = 19 °C and T_{surr} = 15 °C, but was single phase under all other conditions studied.

Averaged propagators $\overline{P}(Z, \Delta)$, the probability of a displacement $Z = z(\Delta) - z(0)$ in time Δ, for the same flow conditions used in the velocity maps were taken to observe the displacement time dependent flow dynamics. In order to compare directly with the velocity map data, propagators were taken at a flow of 0.5 mL/min and pressures of P = 25, 29, and 45 bar with T_{fluid} = 21 °C, T_{surr} = 21 °C, and at displacement observation times of Δ = 10 ms (Fig. 5a) and Δ = 100 ms (Fig. 5b). The experiments used a gradient pulse duration δ = 1 ms and a maximum gradient value of g = ±0.945 T/m in

the axial vertical z-direction of the flow. The propagator curves are plotted as probability of velocity $\overline{P}\left(\frac{Z}{\Delta}\right)$ vs. velocity $\left(\frac{Z}{\Delta}\right)$ and they are an ensemble average of the flow statistics through the cross section of the tubing with a slice thickness of 15 mm. In contrast to the behavior seen in normal liquids in capillary flow in which $\overline{P}(v)$ varies from a hat function at short times due to the equal probability of velocity in the parabolic velocity distribution to a Gaussian at long $\left(\Delta \gg \frac{R^2}{D_o}\right)$ times [35,42], the propagators are near Gaussian at 10 ms and transition to non Gaussian. At 10 ms the diffusion length scale is $l_D \sim \sqrt{2D_o\Delta}$ = 49.6, 31.7, and 18.4 μm for P = 25, 29, and 45 bar, based on the NMR measured molecular diffusivity D_o = 1.23 × 10^{-7}, 5.02 × 10^{-8}, and 1.7 × 10^{-8} m²/s at each pressure, respectively. This is of the same order of magnitude as the advection length scale $l_v = \langle v \rangle \Delta$ = 34.8, 29.2, and 34.4 μm. Transport processes in capillary flow of supercritical and critical fluids is strongly dominated by random diffusive motions at displacement timescales on the order of 10 ms in contrast to ordinary liquids. At longer displacement time Δ = 100 ms the system is still far from the Taylor hydrodynamic dispersion regime for which $\frac{R^2}{D_o} \sim 4.5$, 7.6, and 26.4 s for P = 25, 29, and 45 bar, respectively. The propagators at 100 ms reflect the advection dynamics of the C_2F_6 molecules since now $l_D \sim 161.2$, 123.3, and 66.3 μm and $l_v \sim 290$, 227, and 354 μm. The near critical gas at P = 25 bar and the critical fluid P = 29 bar have a probability peaked toward slower velocity while the supercritical fluid P = 45 bar has higher probability of maximum velocity. The fluid compressibility due to the critical phase transition dynamics at P = 29 bar narrows

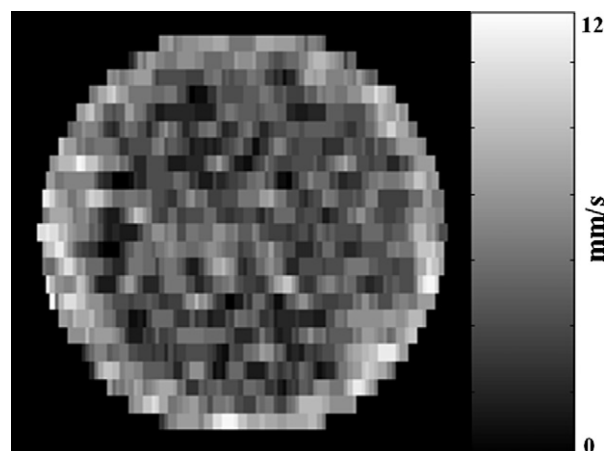**Fig. 6.** Velocity map of C_2F_6 at 0.5 mL/min with an observation time of 2.239 ms in 55 μm beads contained in a 1.5 mm ID capillary at 45 bar.
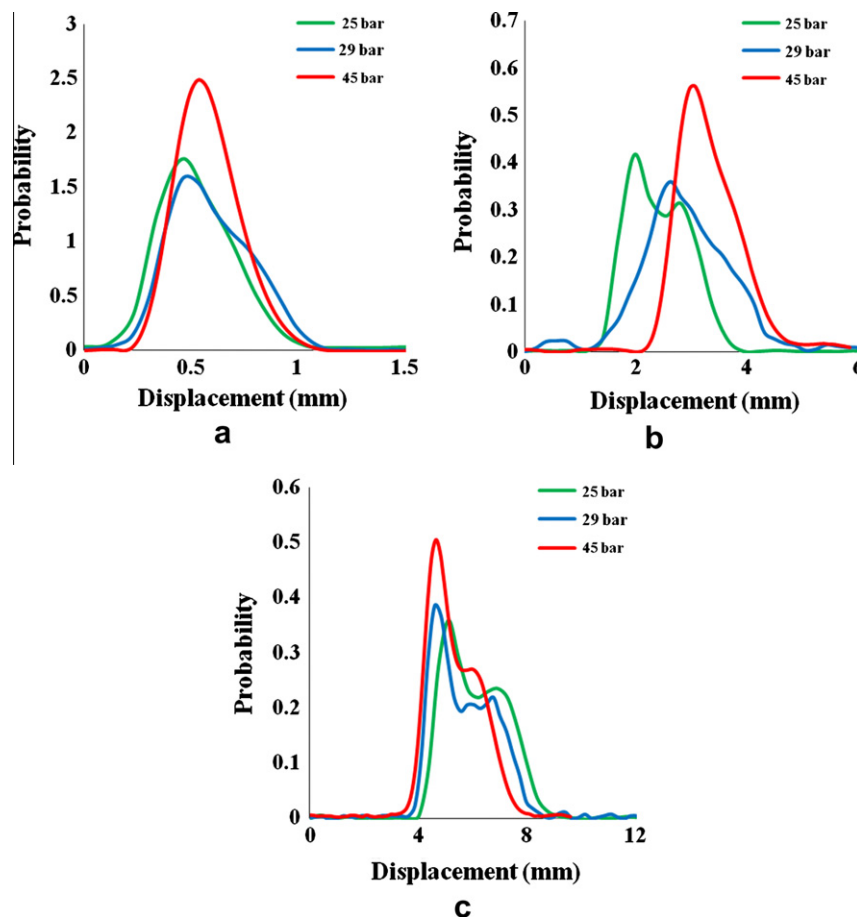
Fig. 7. Propagators (sPGSE) of C_2F_6 at 0.5 mL/min flow through 55 μm beads contained in 1.5 mm ID capillary at (a) 25 bar, (b) 29 bar, and 45 bar for observation times of 50, 300, and 500 ms.

the propagator generating less axial spreading as occurs in Taylor dispersion where the hydrodynamic dispersion scales as $D^* = \frac{\langle v \rangle^2 R^2}{48 D_o}$ and D_o is larger, narrowing $\overline{P}(Z, \Delta)$ due to the phase transition fluctuations.

3.2. Porous media flow

The data represent the first non-invasive spatially resolved velocity measurement of supercritical fluid flow in a porous media, see Fig. 6. At the short displacement observation time $\Delta = 2.239$ ms $l_v \sim 112.9$ μm and $l_D \sim 54.4$ μm. The velocity maps show that the diffusive length scale is of the same order of magnitude as the velocity length scale.

In normal fluids the propagators from bead packs undergo an evolution with displacement time Δ from a near Cauchy like distribution at short Δ relative to the time to traverse a pore by translational motion, i.e. $\tau_v = \frac{l_p}{v_s}$ the ratio of the effective pore length scale l_p and $v_s = \frac{\langle v \rangle}{\Phi}$, to a Gaussian distribution of displacements after multiple pores are traversed and hydrodynamic dispersion dominates [40,41,43]. The propagators for the near critical gas $P = 25$ bar and the supercritical fluid $P = 45$ bar follow a similar displacement time evolution to one another but drastically different than normal fluids. A distinct bimodal distribution is present at longer displacement times. The superficial velocity is $v_s = 8.2$ mm/s for both of these fluids so $\tau_v \sim 5$ ms and multiple pores of the structure of the porous media are sampled for all displacement times in Fig. 7. The critical phase transition fluid $P = 29$ bar exhibits different behavior than the other pressures. Strikingly the impact of compressibility, which caused slower mean displacement in the capillary is not evident as

the mean displacement in the porous media is of similar magnitude to the near critical gas and supercritical fluid. The $P = 29$ bar propagator undergoes a transition with displacement time from a distribution with more skew towards higher displacement than the other fluids at $\Delta = 50$ ms. At $\Delta = 300$ ms $P = 25$ and 45 bar are clearly bimodal by this time and $P = 29$ bar becomes bimodal at $\Delta = 500$ ms similar to the other pressures.

4. Conclusions

MR Velocity maps and propagators of supercritical flow in capillaries and porous media have been measured for the first time. Non-invasive MR has been demonstrated as a useful method in revealing the flow dynamics of fluids in the supercritical region. Buoyancy effects due to small variations in temperature strongly influence velocity distributions. Supercritical C_2F_6 was shown to be very sensitive to a small temperature gradient caused by a slightly warmer tube wall (<1 °C). This sensitivity caused the fluid near the walls to flow faster than that in the center of the tube causing an "M" shape profile demonstrating control of hydrodynamics via thermodynamics. Flow of supercritical fluid in a homogenous porous media has been shown to be inconsistent with hydrodynamic dispersion of normal fluids in porous media.

Acknowledgments

References

[1] H.E. Stanley, Introduction to phase transitions and critical phenomena, Oxford University Press, New York, 1971.

[2] L.A. Allen, T.E. Glass, H.C. Dorn, Direct monitoring of supercritical fluids and supercritical chromatographic separations by proton nuclear magnetic resonance, Anal. Chem. 60 (5) (1988) 390–394.

[3] K. Albert et al., Online coupling of supercritical-fluid chromatography and proton high-field nuclear-magnetic-resonance spectroscopy, Anal. Chem. 66 (19) (1994) 3042–3046.

[4] F.M. Orr, J.J. Taber, Use of carbon-dioxide in enhanced oil recovery, Science 224 (4649) (1984) 563–569.

[5] R.W. Klusman, Evaluation of leakage potential from a carbon dioxide EOR/sequestration project, Energy Convers. Manage. 44 (12) (2003) 1921–1940.

[6] B. Zappoli, Near-critical fluid hydrodynamics, C. R. Mecanique 331 (10) (2003) 713–726.

[7] A. Onuki, Phase Transition Dynamics, Cambridge University Press, Cambridge, 2002.

[8] P.C. Hohenberg, B.I. Halperin, Theory of dynamic critical phenomena, Rev. Mod. Phys. 49 (3) (1977) 435–479.

[9] M. Barmatz et al., Critical phenomena in microgravity: past, present, and future, Rev. Mod. Phys. 79 (2007) 1–52.

[10] D.A. Beysens, Near-critical point hydrodynamics and microgravity, Mech. 21st Century (2005) 117–130.

[11] L.D. Landau, E.M. Lifshitz, Fluid Mech., vol. 26, Pergamon Press, London, 1959.

[12] A. Onuki, Nonequilibrium phase transitions in extreme conditions: effects of shear flow and heat flow, J. Phys.: Condens. Matter 10 (49) (1998) 11473–11490.

[13] A. Onuki, K. Kawasaki, Fluctuations in non-equilibruim steady states with laminar shear-flow – classical fluids near the critical-point, Suppl. Prog. Theor. Phys. (64) (1978) 436–441.

[14] B. Zappoli, S. Amiroudine, S. Gauthier, Rayleigh-Taylor-like instability in near-critical pure fluids, Int. J. Thermophys. 20 (1) (1999) 257–265.

[15] V.A. Kurganov, A.G. Kaptil'ny, Flow structure and turbulent transport of a supercritical pressure fluid in a vertical heated tube under the conditions of mixed convection – experimental-data, Int. J. Heat Mass Transfer 36 (13) (1993) 3383–3392.

[16] K. Okamoto et al., Transient velocity distributions for the supercritical carbon dioxide forced convection heat transfer, J. Nucl. Sci. Technol. 40 (10) (2003) 763–767.

[17] V.A. Kurganov, A.G. Kaptil'ny, Velocity and enthalpy fields and eddy diffusivities in a heated supercritical fluid flow, Exp. Therm. Fluid Sci. 5 (1992) 465–478.

[18] R.E. Sonntag, C. Borgnakke, G.J. van Wylen, Fundamentals of thermodynamics, John Wiley and Sons, New York, 1998.

[19] P.X. Jiang et al., Experimental and numerical study of convection heat transfer of CO₂ at supercritical pressures in vertical porous tubes, Int. J. Heat Mass Transfer 51 (25–26) (2008) 6283–6293.

[20] S.M. Liao, T.S. Zhao, An experimental investigation of convection heat transfer to supercritical carbon dioxide in miniature tubes, Int. J. Heat Mass Transfer 45 (25) (2002) 5025–5034.

[21] J.H. Bae, J.Y. Yoo, H. Choi, Direct numerical simulation of turbulent supercritical flows with heat transfer, Phys. Fluids 17 (10) (2005).

[22] P.X. Jiang, Y. Zhang, R.F. Shi, Experimental and numerical investigation of convection heat transfer Of CO₂ at supercritical pressures in a vertical mini-tube, Int. J. Heat Mass Transfer 51 (11–12) (2008) 3052–3056.

[23] P.X. Jiang et al., Experimental investigation of flow resistance and convection heat transfer of CO₂ at supercritical pressures in a vertical porous tube, J. Supercrit. Fluids 38 (3) (2006) 339–346.

[24] M. Dvoyashkin, R. Valiullin, J. Karger, Supercritical fluids in mesopores–new insight using NMR, Adsorpt. J. Int. Adsorpt. Soc. 13 (3–4) (2007) 197–200.

[25] M. Dvoyashkin et al., Direct assessment of transport properties of supercritical fluids confined to nanopores, J. Am. Chem. Soc. 129 (34) (2007) 10344–10345.

[26] T. Suekane et al., Application of MRI in the measurement of two-phase flow of supercritical CO₂ and water in porous rocks, J. Porous Media 12 (2) (2009) 143–154.

[27] M. Maiwald et al., On-line H-1 NMR spectroscopic investigation of hydrogen bonding in supercritical and near critical CO₂-methanol up to 35 MPa and 403 K, J. Supercrit. Fluids 43 (2007) 267–275.

[28] C.R. Yonker, J.C. Linehan, The use of supercritical fluids as solvents for NMR spectroscopy, Prog. Nucl. Magn. Reson. Spectrosc. 47 (1–2) (2005) 95–109.

[29] P. Etesse, J.A. Zega, R. Kobayashi, High pressure nuclear magnetic resonance measurement of spin-lattice relaxation and self-diffusion in carbon-dioxide, J. Chem. Phys. 97 (3) (1992) 2022–2029.

[30] M.M. Hoffmann, M.S. Conradi, Are there hydrogen bonds in supercritical water, J. Am. Chem. Soc. 119 (16) (1997) 3811–3817.

[31] K. Krynicki et al., Nuclear-spin-lattice relaxation due to critical fluctuations in fluids, Commun. Phys. 1 (6) (1976) 183–189.

[32] B. Newling, Gas flow measurements by NMR, Prog. Nucl. Magn. Reson. Spectrosc. 52 (2008) 31–48.

[33] E.O. Stejskal, J.E. Tanner, Spin diffusion measurements: spin echoes in the presence of a time-dependent field gradient, J. Chem. Phys. 42 (1965) 288.

[34] P.T. Callaghan, Principles of Nuclear Magnetic Resonance Microscopy, Oxford University Press, New York, 1991.

[35] S.L. Codd et al., Taylor dispersion and molecular displacements in poiseuille flow, Phys. Rev. E 60 (4) (1999) R3491–R3494.

[36] K. Saikawa et al., Determination of the critical-temperature and density of hexafluoroethane, J. Chem. Eng. Data 24 (3) (1979) 165–167.

[37] D.O. Kuethe, T. Pietrass, V.C. Behr, Inert fluorinated gas T-1 calculator, J. Magn. Reson. 177 (2) (2005) 212–220.

[38] E.W. Lemmon, M.O. McLinden, D.G. Friend, in: W.G.M. P. J. Linstrom (Ed.), Thermophysical Properties of Fluid Systems in NIST Chemistry Webbook, NIST Standard Reference Database, vol. 69, Gaithersburg, MD 20899: National Institute of Standards and Technology.

[39] H. Madani et al., Vapor-liquid equilibrium data for the (hexafluoroethane + 1,1,1,2-tetrafluoroethane) system at temperatures from 263 to 353 K and pressures up to 4.16 MPa, Fluid Phase Equilib. 273 (1–2) (2008) 92 (vol. 268, 2008, p. 68).

[40] J.D. Seymour, P.T. Callaghan, Flow-Diffraction structural characterization and measurement of hydrodynamic dispersion in porous media by PGSE NMR, J. Magn. Reson. Ser. A 122 (1996) 90–93.

[41] J.D. Seymour, P.T. Callaghan, Generalized approach to NMR analysis of flow and dispersion in porous media, Aiche J. 43 (8) (1997) 2096–2111.

[42] P.T. Callaghan, S.L. Codd, J.D. Seymour, Spatial coherence phenomena arising from translational spin motion in gradient spin echo experiments, Concepts Magn. Reson. 11 (1999) 181–202.

[43] S.L. Codd, S.A. Altobelli, A PGSE study of propane gas flow through model porous bead packs, J. Magn. Reson. 163 (2003) 16–22.